International Journal of Mechanical Sciences 286 (2025) 109913

Contents lists available at ScienceDirect

International Journal of Mechanical Sciences

journal homepage: www.elsevier.com/locate/ijmecsci

Mitigating surface notches for enhanced fatigue performance of metallic gyroid structures via contour scanning

Liming Huang [a], Hongyuan Wan [a], Quanfeng Han [a], Jianxiang Wang [a,b,*], Xin Yi [a,b,*]

[a] Department of Mechanics and Engineering Science, College of Engineering, Peking University, Beijing 100871, PR China
[b] HEDPS, Center for Applied Physics and Technology, Peking University, Beijing 100871, PR China

ARTICLE INFO

Keywords:
Selective laser melting (SLM)
lattice structures
fatigue
surface modification
cyclic ratcheting
micro-CT

ABSTRACT

Additive manufacturing has enabled the creation of lattice structures with tunable properties, making them increasingly popular across various industries. However, their fatigue resistance remains a critical concern for long-term use. While contour scanning, a remelting technique in selective laser melting, improves surface quality and mechanical properties in tensile specimens, its effect on the fatigue behavior of as-built lattices remains underexplored. This study characterizes the manufacturing defects and intricate geometry of 316L skeletal gyroid lattice structures and investigates the impact of contour scanning on their compression-compression fatigue behavior through experimental and numerical approaches. The results show a significant improvement in high-cycle fatigue endurance due to contour scanning, attributed to enhanced surface smoothness. Cyclic ratcheting is identified as the dominant fatigue mechanism in both gyroid samples, with and without contour scanning. Additionally, fatigue life predictions based on finite element analysis, informed by experimental fatigue data and Basquin's equation, align well with experimental results. This work underscores the importance of contour scanning in enhancing the fatigue performance of lattice structures.

1. Introduction

Periodic lattice structures, comprised of arranged struts or skeletons, offer unique properties like lightweight design, high specific stiffness, and effective acoustic or vibration damping [1,2]. Additive manufacturing techniques like selective laser melting (SLM) enable fabrication of complex metallic lattices [3,4], and these structures find applications in aerospace, automotive, and biomedical fields [3,5]. Triply periodic minimal surfaces (TPMS), with zero surface curvature, are particularly interesting due to their potential advantages such as excellent energy absorption and tunable acoustic bandgaps [6,7]. In general, TPMS structures come in two forms: skeletal structures (filling the volume surrounded by the minimal surface) and sheet structures (thickening the minimal surface) [8–10].

While polymeric TPMS structures have been explored, their use is limited by the low strength and ductility of many polymers with brittle tendencies [11,12]. This necessitates research into metallic lattice structures [13,14]. However, complex deformation mechanisms in metals pose challenges. Experimental studies on the relationship between mechanical behavior and topology of steel TPMS indicate that sheet TPMS exhibits stretching-dominated deformation, while skeletal TPMS shows bending-dominated behavior [8]. Additionally, gyroid TPMS structures demonstrate superior elastic properties and more stable responses compared to conventional beam lattices under various loading directions [15]. Further research on dynamic compression suggests that sheet gyroid structures with a higher relative density (over 20 %) exhibit more uniform large deformation under varying strain rates. In contrast, gyroid structures with a 10 % relative density show significant localized deformation at the loading points [16].

The prevalence of cyclic loading in engineering applications necessitates a deep understanding of fatigue properties in lattice structures. Studies have shown that sheet TPMS structures exhibit superior fatigue performance compared to conventional beam-based lattices [17]. Kelly et al. fabricated the sheet gyroid structures and demonstrated that internal pores, strategically introduced through processing parameter adjustments, act as fatigue crack initiation sites rather than the surface roughness [18]. Optimizing these parameters to minimize porosity significantly enhances the fatigue performance of these structures. Mahmoud et al. analyzed effects of manufacturing defects on the compressive fatigue behavior of gradient gyroid structures made from Ti6Al4V, and confirmed that the high fatigue resistance is attributed to its good plasticity, minimal internal porosity, and smaller surface area

* Corresponding authors.
E-mail addresses: jxwang@pku.edu.cn (J. Wang), xyi@pku.edu.cn (X. Yi).

https://doi.org/10.1016/j.ijmecsci.2024.109913
Received 4 June 2024; Received in revised form 18 November 2024; Accepted 25 December 2024
Available online 27 December 2024

[19]. For Ti6Al4V gyroid structures with few internal pores, further research confirmed the role of surface defects in compression fatigue, demonstrating that crack initiation occurs on rough surfaces. This roughness leads to stress concentrations, ultimately weakening the structure's overall fatigue performance [20].

Beyond highlighting the detrimental effects of defects, researchers have also explored methods to optimize fatigue performance. Yang et al. studied the compression fatigue behavior of uniform and gradient Ti6Al4V gyroid structures, observing a clear improvement in fatigue performance for the gradient design [21]. Their simulation results suggest that the lower tensile stress, larger surface areas, and larger microplastic zones in the main load-bearing regions of the gradient structure contribute to this enhancement. Karami et al. investigated the effects of three post-processing methods (hot isostatic pressing, sandblasting, and chemical etching) on the compression fatigue behavior of diamond beam-based lattices [22], and revealed that an optimized combination of these methods led to the highest fatigue resistance.

Metallurgical defects from metal additive manufacturing processes play a critical role in the fatigue behavior of lattice structures. Advances in high-resolution, non-destructive computed tomography (CT), including synchrotron radiation micro-CT (SR-μCT), allow in situ detection and visualization of fatigue damage in metallic materials under various conditions [23–25]. For example, Wu et al. used SR-μCT to investigate high-cycle fatigue in SLM-fabricated Ti6Al4V, revealing that fatigue cracks often initiate at large surface defects, especially lack-of-fusion (LOF) defects, which significantly reduce fatigue life [24]. Qian et al. used in situ CT to explore fatigue crack growth in AlSi10Mg, showing that large, surface-near LOF defects play a dominant role in crack nucleation and coalescence [25].

The above experimental and numerical studies primarily focus on the fatigue behavior of lattice structures made from titanium alloys. In contrast, investigations into the fatigue performance of lattice structures fabricated from other metallic materials remain relatively limited. Nickel-titanium (NiTi) alloy, an intermetallic material renowned for its shape memory effect due to martensite-austenite transformation, has been employed to produce optimized TPMS lattice structures. Fatigue characterization of these structures has identified fatigue damage as the predominant factor influencing their fatigue mechanisms, with fracture surfaces exhibiting pronounced cleavage steps [26].

316L stainless steel, a face-centered cubic (FCC) austenitic steel, is widely used in additive manufacturing due to its excellent balance of strength and ductility. Lattice structures fabricated from 316L exhibit stable and extended plastic plateaus under large compressive deformation, in contrast to the unstable plateaus observed in lattices made from aluminum and titanium alloys [27–29]. This superior compressive performance has drawn attention to the fatigue properties of 316L lattices, though relevant studies remain sparse. Yang et al. investigated the enhancement of compression-compression fatigue performance in 316L gyroid structures fabricated by SLM through sandblasting. This treatment reduced adhered surface defects and introduced a subsurface compressive stress region, thereby improving fatigue behavior [30]. Given the inevitability of manufacturing defects, optimizing defect distribution has also emerged as a key research focus for enhancing the fatigue performance of fabricated 316L lattices.

Recent studies have examined various scanning strategies and their effects on the microstructure and mechanical properties of SLM-fabricated specimens [31]. Contour scanning, a surface modification technique, has been shown to improve density, surface quality, and mechanical properties in tensile test specimens [32–34]. However, its impact on fatigue resistance in both as-built bulk specimens and lattice structures remains largely unexplored. While Plessis et al. acknowledged the negative impact of rough surfaces without contour scanning on fatigue properties in Ti6Al4V gyroid structures, their study focused on internal porosity [35]. Their findings highlight the need for further investigation into the potential benefits of contour scanning, particularly for high surface area structures like gyroid lattices. Given the strong compressive performance of 316L lattices, more detailed investigations into the effects of contour scanning and fatigue mechanisms are essential for supporting their long-term applications.

In this work, we aim to explore effects of contour scanning on the fatigue property of 316L gyroid skeletal structures fabricated via SLM. Fabricating dogbone-shaped specimens, inclined struts, fatigue tensile bars, and gyroid structures, their mechanical behavior and microstructure are experimentally characterized to elucidate roles of material properties, surface roughness, and structure geometry on the fatigue of the gyroid structures. Experimental results demonstrate a remarkable improvement in the high-cycle fatigue life of gyroid structures with contour scanning, exhibiting roughly three times the lifespan compared to those fabricated without it. Cyclic ratcheting is identified as the dominant fatigue mechanism. Furthermore, by incorporating experimental fatigue life data from fatigue bars and the fitted Basquin's equation, finite element analysis successfully predicts the fatigue life of the gyroid structures without and with contour scanning, demonstrating good agreement with fatigue testing.

2. Materials and fabrication

Powder particles of 316L stainless steel are used for the SLM process, and a nominal chemical composition of the powder is listed in Table 1. The particle size falls in a range between 15 μm and 53 μm. All specimens, including tensile specimens, inclined struts, fatigue tensile bars, and gyroid TPMS lattice structures (Fig. 1a), are fabricated using an SLM® 125HL machine (SLM Solutions Group AG, Germany) with the SLM chamber filled with high purity argon atmosphere to prevent powder oxidation during manufacturing. A stainless steel substrate plate is used and preheated to 200 °C. Each powder layer is applied with a thickness of 30 μm, and the scanning direction is rotated by 33° between layers. The scanning pattern for each layer is divided into stripes, filled using a zigzag hatch approach. For contour scanning, a single contour pass is applied for each layer without overlap or gaps between the contour and the end of the hatch track. The primary manufacturing parameters for hatch scanning are optimized to minimize porosity in bulk parts, with a laser power of 200 W, a scanning speed of 800 mm/s, and a hatch spacing of 120 μm. In contour scanning, the laser power and scanning speed are adjusted to 100 W and 400 mm/s, respectively, to remelt the slice boundary and improve surface quality. A summary of these manufacturing parameters is provided in Table 2.

In this work, we aim to understand the fatigue property of the gyroid TPMS lattice structures with as-built rough surfaces, and our experiments detailed in following discussion indicate that fatigue failure occurs on ligaments of the lattice structures. To elucidate roles of mechanical properties of materials, surface roughness, and structure geometry on the fatigue behavior of the gyroid structures, several components are fabricated. The dogbone-shaped tensile specimens are cut from the SLM-fabricated block specimens and are used to obtain the tensile true stress-strain curve in uniaxial tensile tests. The inclined struts are used to characterize the surface roughness and microdefects. The fatigue tensile bars and gyroid structures are used in fatigue experiments. Based on mechanical properties of the tensile specimens, finite element analysis is performed to determine the true stress response in the gyroid structures. Combined with fatigue properties of tensile bars, fatigue endurance cycles of the gyroid structures are estimated. All specimens are in their as-built states, and no heat treatments are applied.

To reveal the effects of surface appearance on the fatigue of the SLM-fabricated specimens, two different scanning strategies are used: (1) stripe scanning and (2) stripe scanning followed by contour scanning (Fig. 1b). These two scanning strategies are applied for inclined struts, fatigue tensile bars, and gyroid TPMS lattice structures. No contour scanning is applied for the SLM-fabricated block specimens. All fabricated specimens are cleaned in an ultrasonic bath before mechanical testing.

The lattice structure in this work is generated from the Schoen's

Table 1
Nominal chemical composition of the 316L stainless steel powder (wt. %).

Cr	Ni	Mo	Mn	Si	O	C	P	S	Fe
16.67	10.59	2.64	0.7	0.28	0.063	0.013	0.009	0.004	Balance

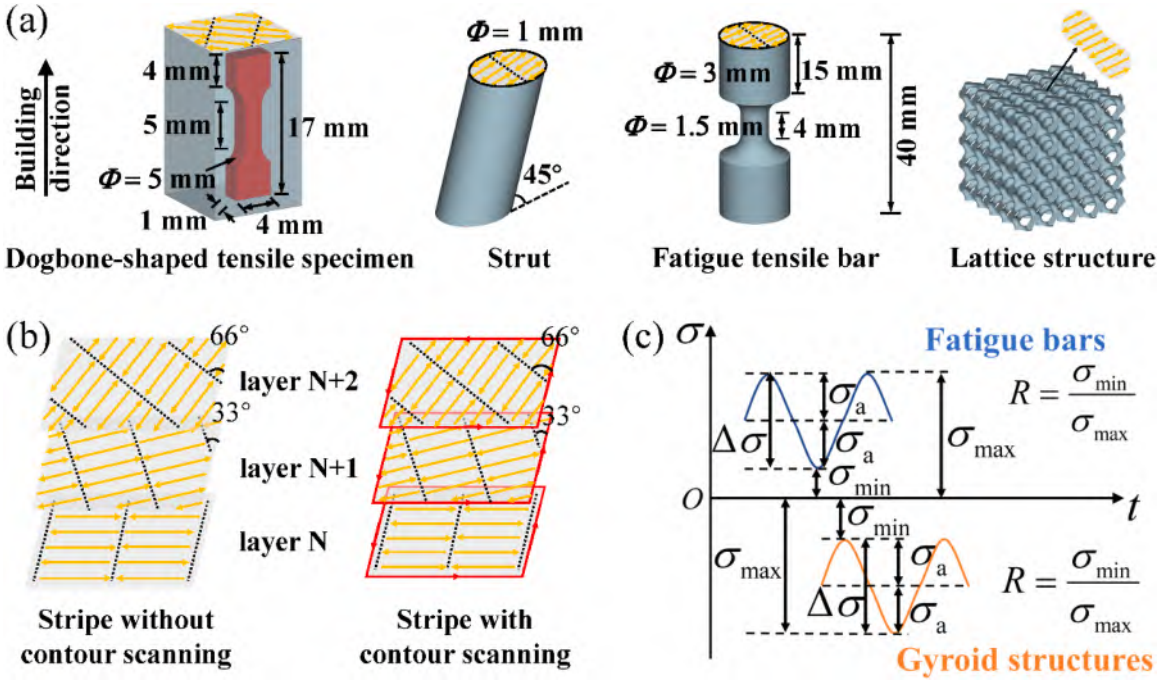

Fig. 1. Schematics of laser scanning strategies used for the specimen fabrication by SLM (a,b) and cyclic loading (c). (a) Illustration of SLM-fabricated specimens considered in this work, including dogbone-shaped tensile specimen (in red) cut from SLM-fabricated blocks of rectangular cross-sections, inclined struts of roughly elliptical cross-sections, fatigue tensile bars of circular cross-sections, and gyroid TPMS lattice structures. The lattice structure is composed of 5 × 5 × 5 unit cells. (b) Scanning strategies: stripe scanning and stripe scanning (yellow lines) followed by contour scanning (red lines). (c) Sinusoidal cyclic loading from a tensile stress on fatigue bars to a nominal compressive stress on gyroid structures ($\Delta\sigma$, stress range; σ_a, stress amplitude; σ_{max}, maximum stress; σ_{min}, minimum stress; R, stress ratio).

Table 2
Main processing parameters for SLM-fabricated specimens.

	Laser power	Scanning speed	Hatch spacing
Stripe scanning	200 W	800 mm/s	120 μm
Contour scanning	100 W	400 mm/s	90 μm

gyroid TPMS and its shape is described by the following implicit surface representation

$$\sin\frac{2\pi x}{L}\cos\frac{2\pi y}{L}+\sin\frac{2\pi y}{L}\cos\frac{2\pi z}{L}+\sin\frac{2\pi z}{L}\cos\frac{2\pi x}{L}=c,$$

where L is the unit cell size and the parameter c regulates the volume surrounded by the gyroid surface. In this study, $L = 4$ mm and the gyroid unit cell is of relative density 20 % with $c = 0.902$. The lattice sample consists of a 5 × 5 × 5 array of unit cells, resulting in a lateral dimension of 20 mm × 20 mm.

3. Mechanical and morphological characterizations

3.1. Uniaxial tensile testing with dogbone-shaped specimens

To determine the mechanical properties of the 316L stainless steel, dogbone-shaped tensile specimens, cut from the SLM-fabricated block specimens, are used in tensile tests for true stress-strain curves. The uniaxial tensile tests at room temperature of three dogbone-shaped tensile specimens are performed at a nominal strain rate of 5×10^{-4} s^{-1} using an electromechanical tensile testing machine (CMT4204, MTS). The loading direction is parallel to the building direction. The true stress-strain curves are shown in Fig. 2. Values of mechanical properties of 316L stainless steel, such as Young's modulus E of 180 GPa and yield strength of 522 MPa, from Fig. 2 are then used in the later finite element simulations to determine the true stress and strain fields of deformed lattice structures.

3.2. Surface roughness characterization of inclined struts

Due to the challenge of directly quantifying the surface roughness of TPMS structure ligaments, we address this limitation by constructing inclined struts with an identical inclination angle (the angle between the

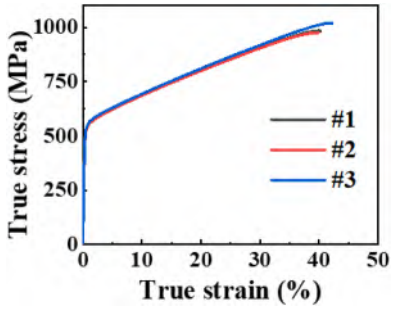

Fig. 2. True stress-strain (σ^t-ε^t) curves of three SLM-fabricated 316L specimens with a Young's modulus E of 180 GPa and yield strength of 522 MPa.

strut axis and the building platform plane, 45° angle in Fig. 1a) to that of the TPMS ligaments of comparable size. We then conduct surface roughness characterization on these inclined struts for estimating the ligament surface roughness. No mechanical testing is performed with the struts. Surface morphologies of the struts and gyroid specimens are imaged using Quanta 200F and Nova Nano 430 scanning electron microscope (SEM) (FEI, USA) under 10 kV~20 kV. Additionally, surface defects of the inclined struts are characterized using a high-precision CT system (SkyScan 1272, Bruker Corporation, Belgium) operated at 100 kV and 80 μA. For each specimen, projections are collected at 0.3° increments over a 180° rotation, with an exposure time of 3.46 s per projection. The resulting tomography dataset, with $892 \times 892 \times 1040$ voxels and an isometric voxel size of 3 μm, captures the entire 3 mm gauge length of each strut. Grayscale radiographs are reconstructed using the filtered back projection algorithm, followed by 3D median filtering for noise reduction and interactive thresholding for segmentation. The volume-rendered data allows visualization and detailed analysis of surface defect distributions.

Fig. 3a,b shows surface geometries of two inclined struts reconstructed with CT detection results. The strut without contour scanning has a higher roughness in comparison with that with contour scanning. To further quantify the surface roughness, surface profiles of the longitudinal sections are extracted at 10° intervals around the struct circumference, with representative profiles shown in Fig. 3c. In total, 36 surface profiles are obtained for each strut. The arithmetic average roughness R_a (mean height of a profile line) and the maximum peak-to-valley height R_t (difference between the maximum and minimum profile heights) [36] of each strut are calculated based on these surface profiles. For the strut without contour scanning, $R_a = 23.30$ μm and $R_t = 155.3$ μm; for the strut with contour scanning, both average roughness and maximum height are reduced ($R_a = 17.88$ μm and $R_t = 124.2$ μm). Deviations of the average roughness and maximum height, with R_a and R_t as the baselines, are illustrated in Fig. 3d, indicating that the surface roughness of individual profiles is more uniformly distributed with smaller deviations when contour scanning is applied.

3.3. High-cycle fatigue testing with fatigue bars

For the fatigue tensile bars, high-cycle fatigue tests are conducted utilizing an electronic testing device (Instron ElectroPlus E1000, USA) via a sinusoidal tensile loading at a frequency of 30 Hz and a stress ratio R (the minimum stress divided by the maximum stress) of 0.1. The

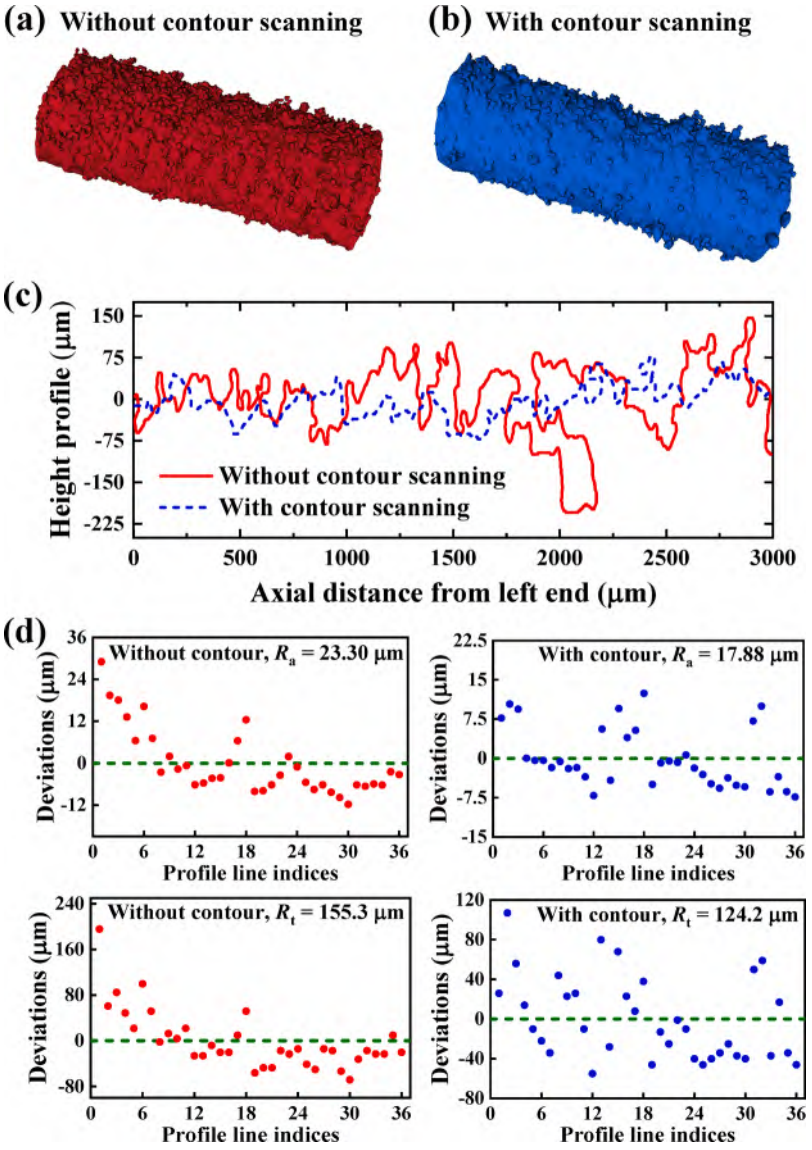

Fig. 3. (a,b) Surface reconstruction from CT scans of the struts without and with contour scanning. (c) Height profiles of selected longitudinal sections of the struts. (d) Profile deviations from the baselines.

fatigue life is defined as cycle counts for the complete rupture of the fatigue tensile bars [37]. With knowledge of fatigue properties of the fatigue tensile bars from experiments, the fatigue life prediction of gyroid lattice structures could be performed.

Fig. 4 shows the fatigue life cycles of the tensile bars without and with contour scanning at a stress ratio $R = 0.1$. The tensile bars with contour scanning exhibit higher fatigue cycles in comparison with those without contour scanning, indicating that contour scanning indeed enhances the fatigue property of the as-built samples. Fractography is conducted to reveal the mechanisms underlying the fatigue crack initiation and propagation (Fig. 5). For tensile bars without and with contour scanning, fatigue cracks in the loading regime of the high-cycle fatigue originate from surface defects regardless of the applied nominal stress. Initial surface defects, marked with dashed lines in Fig. 5, indicate that opening notches and partially melted powders on the bar surfaces or sub-surfaces act as initiation sites for fatigue cracks. The crack initiation regions in the tensile bars with contour scanning have more regular shapes like narrow stripes parallel to the surface contour. In contrast, the crack initiation regions of the bars without contour scanning have sharp corners, indicating that the notches facilitate the crack initiation and reduce the fatigue resistance. Moreover, the crack initiation induced by the internal pores is not observed for all fatigue tensile bars, suggesting that surface defect is the decisive factor in determining the fatigue life of tensile bars here.

4. Microstructural characterization and fatigue properties of the gyroid TPMS lattice structures

In Section 3, we have estimated mechanical properties of SLM-fabricated 316L components, surface roughness of ligament-shaped struts, and fatigue properties of bar-shaped components, and several components are characterized. Now we investigate microstructure and fatigue properties of the SLM-fabricated gyroid TPMS lattice structures.

4.1. Surface morphologies

Fig. 6 shows SEM images of surfaces of the lattice structures with and without contour scanning, on which significant accumulation of metallic powders, including partially melted ones, could be observed. The lattice structures without contour scanning have more surface microcracks and voids in comparison with these with contour scanning. As shown in Fig. 6d-f (the rightmost column), some accumulated or unmelted particles still exist on the strut surfaces with contour scanning. The staircase effect, characterized by a ladder-like appearance resulting from distinct boundaries between adjacent layers during layer-by-layer construction, is visible in Fig. 6f for the structures with contour scanning, where mild powder accumulation is present [38]. Overall, the surface quality of the gyroid lattice structures is significantly improved with contour scanning.

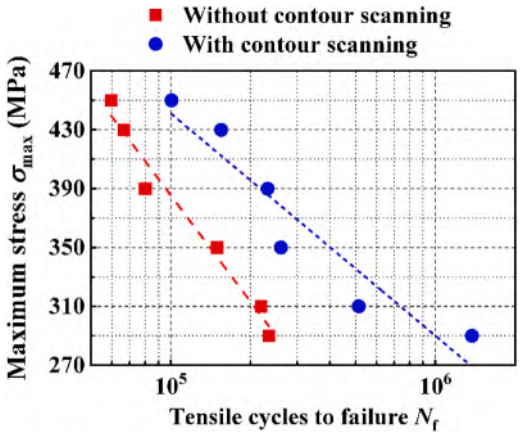

Fig. 4. Tensile cycles to failure of the tensile bars without and with contour scanning at a stress ratio $R = 0.1$.

To further evaluate the surface features of the lattice structures, CT dimensional measurements and reconstruction of unit lattice cells are conducted with nanoVoxel-3000 (Sanying Precision Instruments Company, China). The CT system is operated at 150 kV with a tube current of 60 μA, collecting 1440 projections over a 360° rotation with an exposure time of 0.35 s per scan. The resulting tomography data, processed and visualized with a resolution of 2400 × 2400 × 2200 voxels and an isometric voxel size of 3.15 μm (Fig. 7a,b), reveals rough surfaces with powder accumulation and no structure distortion, consistent with SEM results in Fig. 6. The lattice structures without contour scanning have more severe powder accumulation in comparison with these with contour scanning, as marked by red elliptic circles. With the surface deviation extent quantified using the nearest neighbor distance between the CT-based point data and the ideal model, Fig. 7c,d shows the contour difference between the designed ideal model and the reconstructed surface of the unit cells, with red and blue regions indicating the oversize and downsize defects of the reconstructed model, respectively. As indicated in Fig. 7c,d, the unit cell with contour scanning exhibits superior geometrical consistency with the ideal model in the inclined struts, in contrast to the unit cell without contour scanning. Statistical distributions of the surface deviations resemble the Gaussian distribution and the unit cell with contour scanning has a more concentrated distribution (Fig. 7e,f). For the unit cells without and with contour scanning, the statistical surface areas are 102.9 mm^2 and 78.9 mm^2, respectively, in contrast to the ideal surface area 59.8 mm^2, suggesting the surface without contour scanning exhibiting more roughness.

For the gyroid structures examined in this study, maximum geometric deviations are observed around the overhanging regions in both cases, with and without contour scanning. Since the bulk material has substantially higher thermal conductivity than the surrounding loose powder, heat accumulation in overhanging areas results in the formation of larger melt pools [39]. These pools transport partially melted particles from prior layers, leading to pronounced surface distortions. In horizontal overhanging regions, surface defects appear oversized but have minimal impact on mechanical performance, as they are located in struts oriented perpendicularly to the loading direction. In contrast, inclined struts with down-facing areas exhibit more significant surface defects, particularly in the absence of contour scanning, where these distortions may deteriorate mechanical properties and serve as fatigue crack initiation sites in the gyroid lattice. Additionally, due to the layer-wise fabrication and powder-based raw materials, some surface roughness and deviation from the ideal model are inherent in both cases. However, the up-facing areas in inclined struts without contour scanning show greater surface deviations, which further contribute to a reduction in both mechanical strength and fatigue performance.

4.2. Porosity analysis

The fatigue performance of additively manufactured parts is sensitive to surface defects and interior pores, as these defects usually contribute to the initiation and propagation of fatigue cracks. For the analysis of the unit cell porosity, volume rendering visualization based on the CT-reconstructed model is used (Fig. 8). To reduce image noise, only pore defects with volume larger than 10 voxels (312 μm^3) are examined [40]. It is shown that internal pores (red dots in Fig. 8), including lack of fusion defects and gas pores, are few and almost inevitable in the SLM-fabricated unit cells. Moreover, pore defects are mainly located near the strut surfaces. A total of 144 and 127 pore defects are detected for the unit cells without and with contour scanning, respectively. The volume porosity is smaller than 0.01 %. As the laser turns around at the slice boundary, the repeated heating of the track end usually results in the keyhole phenomenon and material evaporation [41], which coincides with the porosity distribution from the CT-reconstructed models.

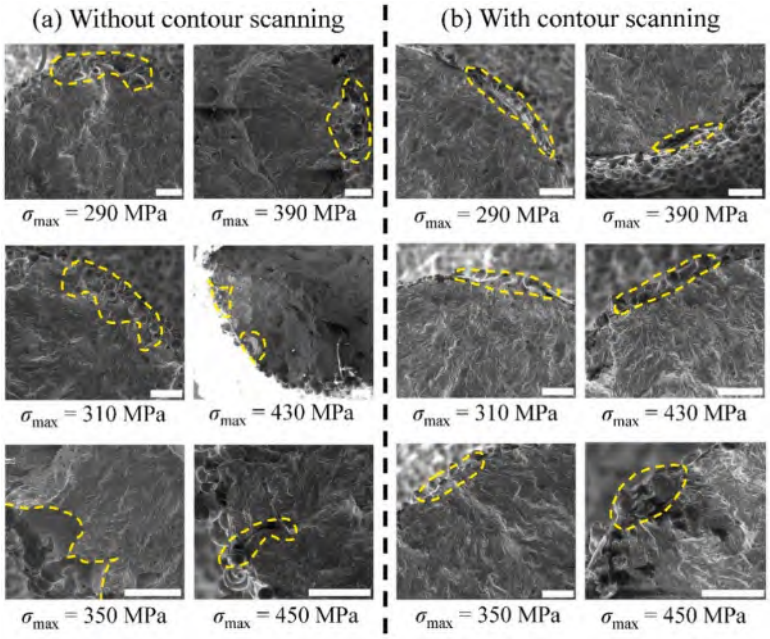

Fig. 5. SEM images of fatigue crack initiation regions on fracture surfaces of the tensile bars without contour scanning (a) and with contour scanning (b) under different values of the maximum applied nominal stress σ_{max}. Dashed outlines indicate initial surface defects. Scale bars, 100 μm.

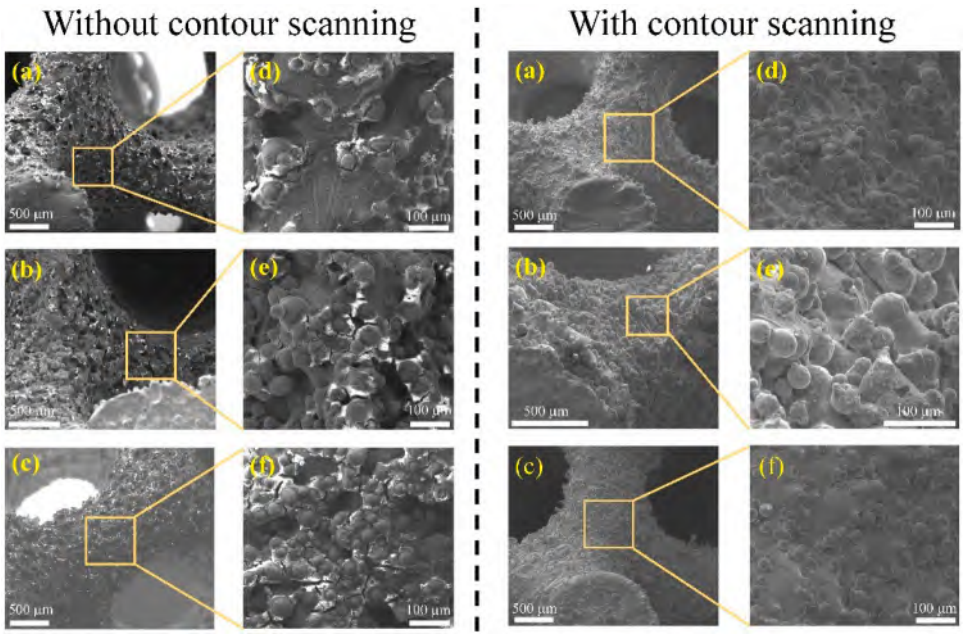

Fig. 6. SEM images of surface morphologies of the gyroid lattice structures without (left two columns) and with (right two columns) contour scanning. (a,d) Top view, (b,e) bottom view, and (c,f) side view.

4.3. Microstructure characterization

Our fatigue testing (discussed later in Section 4.4.2) reveals that fracture in the lattice structures primarily occurs at the inclined struts. To explore the role of strut microstructure in the fatigue performance of gyroid lattice structures, electron backscattered diffraction (EBSD) measurements are employed for microstructural characterization of the inclined struts from the fabricated gyroid unit cells shown in Fig. 7. In Fig. 9a,b, EBSD orientation maps of the inclined struts (the struts circled on the right in Fig. 7a,b) reveal coarser grains primarily within the strut interiors, while finer grains are observed near the strut surfaces. Orientation pole figures indicate an absence of clear texture along the building direction in both samples (Fig. 9a,b). The 33° angle of scanning direction between adjacent building layers contributes to mitigating strong texture along the building direction, and the inclination of struts further reduces texture intensity [30,42]. Due to the lack of a strong texture, the material is treated as isotropic in numerical simulations in Section 5. Statistical distributions of grain size from the EBSD orientation maps show that struts without and with contour scanning share nearly identical grain size distributions (Fig. 9c). This suggests that contour scanning does not induce significant microstructural differences, and microstructure may not be the primary factor influencing the fatigue performance discrepancy between gyroid samples without and with contour scanning.

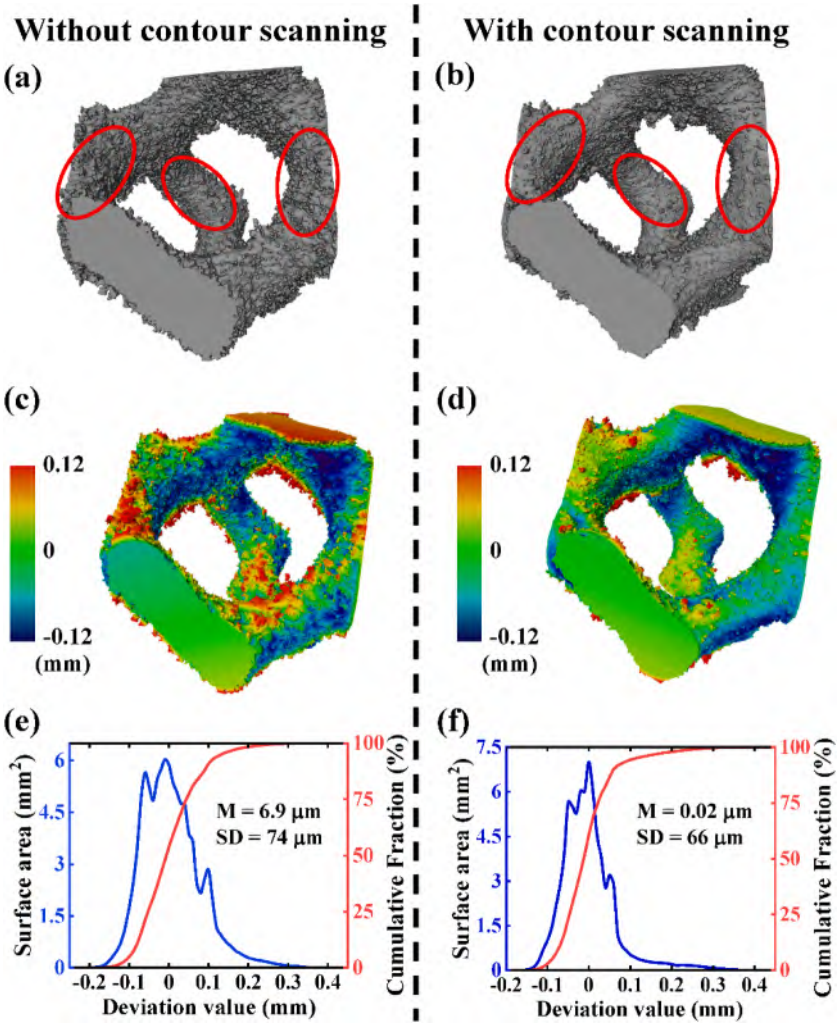

Fig. 7. (a,b) CT-reconstructed surfaces for the as-built unit cells, (c,d) contours deviation between the ideal model and as-built unit cells, and (e,f) statistical distributions of surface deviations with the mean value (M) and standard deviation (SD). (a,c,e) for the case without contour scanning and (b,d,f) for the case with contour scanning. (a,b) are based on grayscale images with an isometric voxel resolution of 3.15 μm.

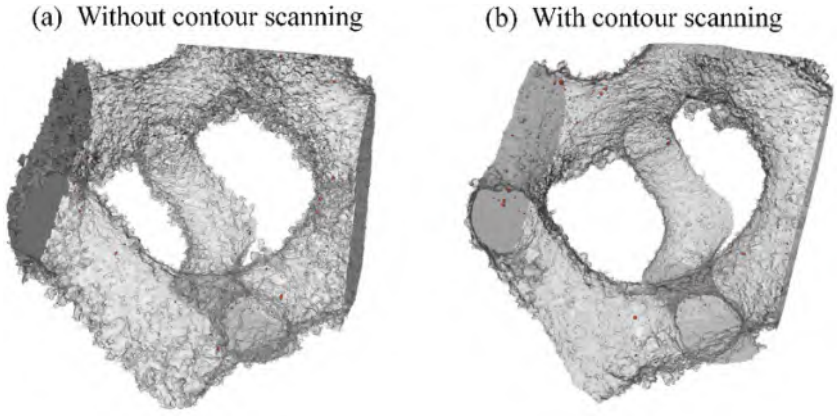

Fig. 8. Volume rendering visualization of unit cells without (a) and with (b) contour scanning. Red regions, internal pores.

4.4. Mechanical properties

Uniaxial compressive tests and compression-compression high-cycle fatigue tests are conducted on gyroid lattice structures, with the loading direction parallel to the building direction, utilizing the MTS servohydraulic test systems (MTS model 370.10 load frame). In the uniaxial compressive tests, a displacement rate of 1.2 mm/min is employed. In the fatigue tests, the cyclic loading of constant frequency 20 Hz and stress ratio $R = 0.1$ is adopted. The end of each fatigue test is determined by monitoring nominal compressive strain via a displacement gauge. When a nominal compressive strain of 12.5 % is reached, a significant reduction in stiffness (over 85 % compared to the initial loading

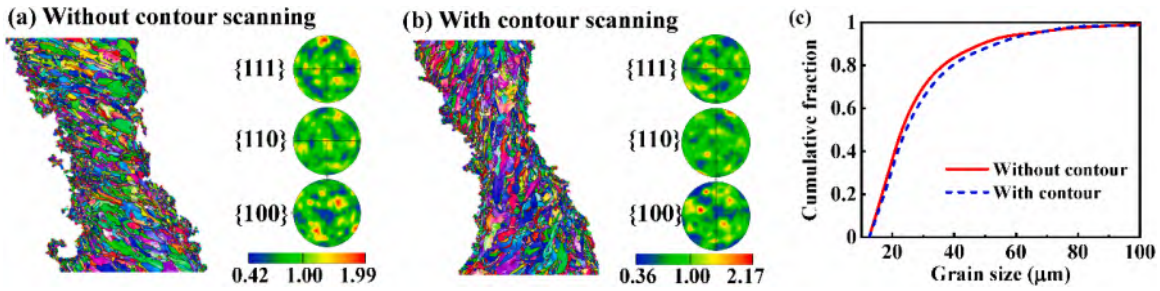

Fig. 9. Orientation maps and orientation pole figures of gyroid samples without (a) and with (b) contour scanning taken from the building direction. (c) Grain size distributions of the gyroid samples.

stiffness) is observed, along with coalescence of fatigue cracks and rupture of the inclined struts. Under these conditions, the samples are considered to have failed. If failure does not occur, the maximum loading cycle is capped at 2×10^6 (run-out limit). Therefore, in this study, the fatigue life of the gyroid structures is defined as the number of cycles required to reach a nominal compressive strain of 12.5 %, and the fatigue strength is defined as the maximum nominal stress σ_{max} applied in the fatigue cycles over 2×10^6. In the following experimental analysis, the nominal compressive stress for a lattice sample is defined as the compressive force divided by the cross-sectional area of the entire gyroid sample perpendicular to the loading direction, which is 20 mm × 20 mm.

4.4.1. *Compressive properties*

Quasi-static compressive tests are first carried out on the gyroid samples of a relative density 20 % to analyze possible discrepancies between samples without and with contour scanning. Representative nominal compressive stress–strain curves for the gyroid samples without contour and with contour are shown in Fig. 10. The nominal stress–strain curves are divided into three regions, a linear elastic region, a long stress plateau and a densification region. As the 316L stainless steel possesses excellent plasticity (Fig. 2), the long plateau remains stable without sudden drops. No obvious strut fractures are observed even in the densification region, different from the compressive process of AlSi10Mg lattices [43]. From the nominal stress–strain curves, the effective Young's modulus as the curve slope in the elastic region, the traditional 0.2 % offset yield strength, and the plateau stress as the arithmetical average of the corresponding nominal stresses between 20 % and 40 % nominal compressive strain can be determined. In comparison with gyroid samples without contour scanning, the samples with contour scanning are of around 30 % higher in the yield strength, 19.8 % higher in the plateau stress. The effective Young's modulus is around 1.1 GPa for the gyroid samples without and with contour scanning. The improved plastic plateau in the gyroid sample with contour scanning can be attributed to the improved damage tolerance from the surface modification.

4.4.2. *Fatigue properties*

Fig. 11a,b presents the hysteretic nominal stress–strain curves for gyroid samples, both without and with contour scanning, under a maximum nominal stress of 16.25 MPa. The gradual rightward shift along the nominal strain axis with increasing cycle number in both samples reveals ratcheting or cyclic creep, a behavior in which plastic deformation accumulates due to asymmetric cyclic mechanical stress. Cyclic ratcheting refers to the progressive accumulation of nominal strain within lattice structures due to the cyclic plastic bending of struts, primarily driven by the applied non-zero mean stress during cyclic fatigue [44,45]. Despite the applied nominal stress being lower than the nominal yield strength of the structure (Fig. 10b), the von Mises stress in certain struts may approach or even exceed the yield strength of 316L material due to the complex geometry and distribution of defects, which accelerates the nominal strain growth rate of the structure and results in localized plastic deformation in these struts. As fatigue cycles increase, this plastic deformation gradually accumulates, leading to the onset of ratcheting behavior.

Additionally, reduction in secant modulus for both curves reflects fatigue crack initiation and propagation during cyclic loading [45–47]. The conspicuous rightward shift in the hysteretic curves for the gyroid sample without contour scanning occurs at the beginning of cyclic loading (Fig. 11a), while the same shift in the gyroid sample with contour scanning becomes visible after 10^5 loading cycles (Fig. 11b). The degradation of the secant modulus is notable after 10^5 cycles for the hysteretic curves without contour scanning and after 4×10^5 cycles for the curves with contour scanning. To differentiate the effects of cyclic ratcheting and fatigue crack growth in the struts during cyclic compression, the nominal cyclic ratcheting strain (or creep strain) and fatigue damage strain are derived in Fig. 11c,d, following the method proposed in Ref. [48]. The nominal cyclic ratcheting strain ε_{rat} and fatigue damage strain ε_{dam} are defined, respectively, as

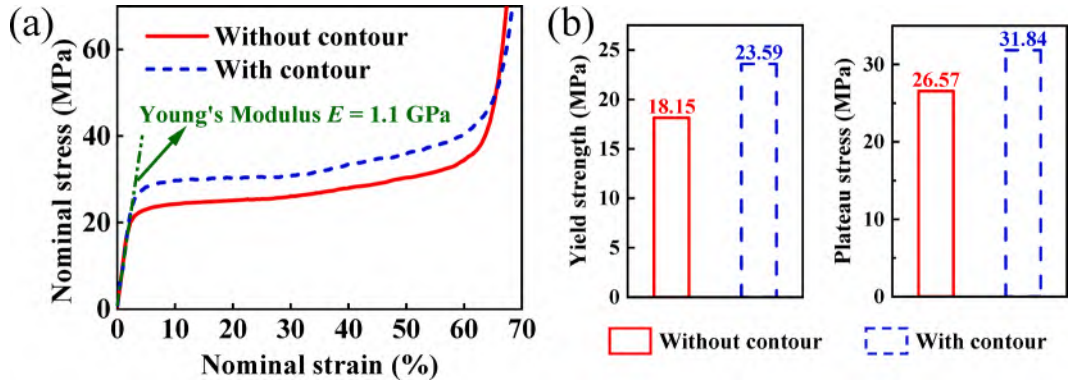

Fig. 10. (a) Representative nominal compressive stress–strain curves of gyroid lattice samples without and with contour scanning. (b) Structure yield strength and plateau stress extracted from the nominal stress–strain curves shown in panel (a).

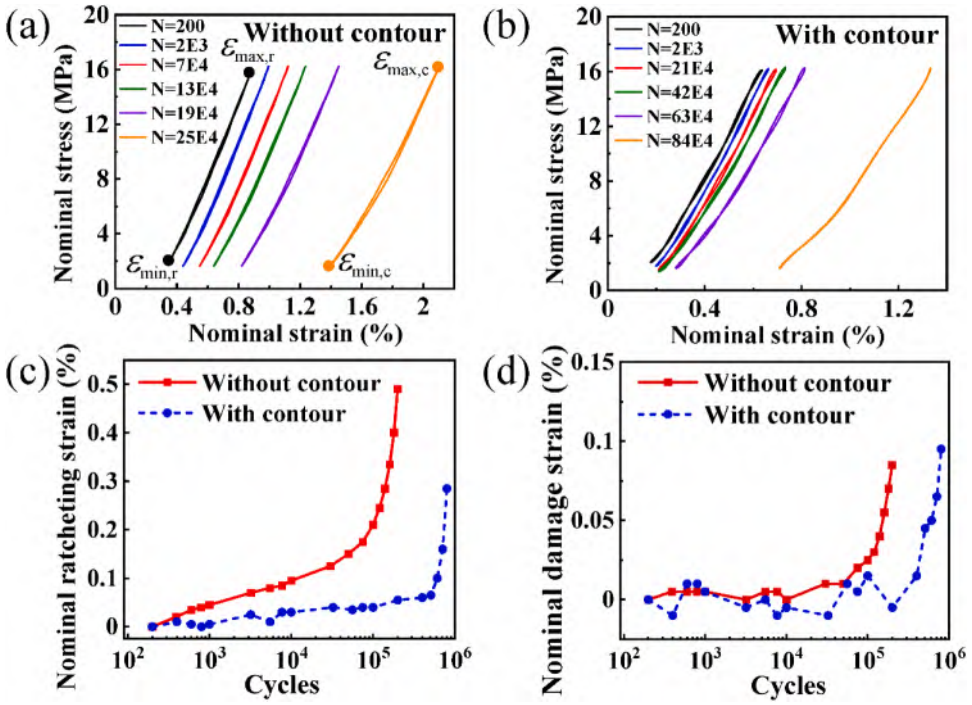

Fig. 11. (a,b) Hysteretic nominal stress–strain curves for gyroid samples without and with contour scanning. (c,d) Corresponding nominal ratcheting strains and fatigue damage strains. *N*, loading cycle number.

$$\varepsilon_{rat} = \varepsilon_{min,c} - \varepsilon_{min,r} \quad \text{and} \quad \varepsilon_{dam} = \varepsilon_{max,c} - \varepsilon_{max,r} - \varepsilon_{rat},$$

where $\varepsilon_{min,c}$ and $\varepsilon_{max,c}$ are the nominal minimum and maximum strains in the current loading cycle (e.g., $N = 2.5 \times 10^5$), respectively, $\varepsilon_{min,r}$ and $\varepsilon_{max,r}$ are the nominal minimum and maximum strains in the reference loading cycle ($N = 200$), respectively.

The fatigue mechanisms of metallic lattice structures have been extensively studied in aluminum, titanium, and steel lattices, revealing two main mechanisms of fatigue failure: cyclic ratcheting and fatigue crack initiation and propagation within the lattice struts. It is reported that compression-compression fatigue in aluminum foams is dominated by strain accumulation through material ratcheting at cell edges, without involvement of cell-edge cracking [44]. However, recent studies on additively manufactured titanium and steel lattices have shown that both cyclic ratcheting and fatigue crack initiation and propagation contribute to fatigue failure behaviors [30,47]. Therefore, the impact of cyclic ratcheting and fatigue damage on fatigue properties depends on the cell structures and the metals used.

As shown by the decoupled nominal strains in Fig. 11c,d, both nominal ratcheting and damage strains exhibit two distinct stages: steady growth and rapid growth. During the steady growth stage, cyclic ratcheting, induced by asymmetric stress cycling (i.e., non-zero mean stress), plays a primary role in the fatigue process, as nominal ratcheting strains are significantly higher than nominal damage strains in both samples. In the rapid growth stage, however, fatigue damage becomes prominent alongside the cyclic ratcheting mechanism, suggesting that fatigue crack propagation in the gyroid samples substantially reduces the structural load-bearing capacity. Overall, cyclic ratcheting emerges as the more significant contributor throughout the fatigue process in these gyroid structures. The onset of rapid growth in both ratcheting and damage strains occurs at a lower cycle count in samples without contour scanning compared to those with contour scanning, indicating that contour scanning significantly enhances fatigue performance.

A prominent feature of metallic cellular structures under compressive cyclic loads is the accumulation of nominal compressive strain [46]. In Fig. 12, the profiles of nominal strains (maximum nominal strain of each hysteretic curve) for gyroid samples under cyclic loads can be roughly categorized into three stages: initial increase in nominal strain within the early cycles ($N < 200$), sustained and more gradual nominal strain growth over an extended cycle period, and abrupt nominal strain accumulation leading to fatigue failure. In the gyroid samples without contour scanning and subjected to high nominal stress surpassing the yield strength of the lattice structures, the distinction between the first and second stages is less apparent. With increasing cyclic nominal stress, the cycle number (N_T) corresponding to the transition from the second to the third stage decreases and fatigue life decreases. Under the same nominal stress, the nominal strain during the steady growth stage for the samples without contour scanning is lower than that for the samples with contour scanning, suggesting that contour scanning enhances compressive deformation resistance.

With knowledge of the relationship between the nominal strain ε and cycle number N, the nominal strain growth rate, $d\varepsilon/dN$, between the 200th cycle and the point N_T can be determined for the gyroid samples under various maximum nominal stresses (Fig. 13a). The value of $d\varepsilon/dN$ increases with increasing maximum nominal stresses in the cyclic loading. Under the same maximum nominal stress, the samples with contour scanning exhibit a notable reduction in $d\varepsilon/dN$, approximately by an order of magnitude compared to the samples without contour scanning. This observation substantiates that the samples with contour scanning possess superior fatigue performance. In Fig. 13b, the maximum nominal stress versus fatigue life illustrates that the fatigue life increases as the nominal stress decreases. Lowering the nominal stress to a specific value results in the fatigue life reaching a limit, corresponding to a loading cycle capped at 2×10^6 (run-out limit). A similar tendency is observed with the fatigue life results for the fatigue tensile bars (Fig. 4). The fatigue life of the samples with contour scanning is substantially improved, highlighting the significant role of surface modification in enhancing fatigue properties of metallic gyroid structures.

Fig. 14 demonstrates macroscale failure behavior of the gyroid samples without and with contour scanning during the compressive fatigue process. At the maximum nominal stress of 13.5 MPa, the gyroid samples without contour scanning show clear 45° fracture bands in the inclined struts; the gyroid samples with contour scanning, in some instances, show

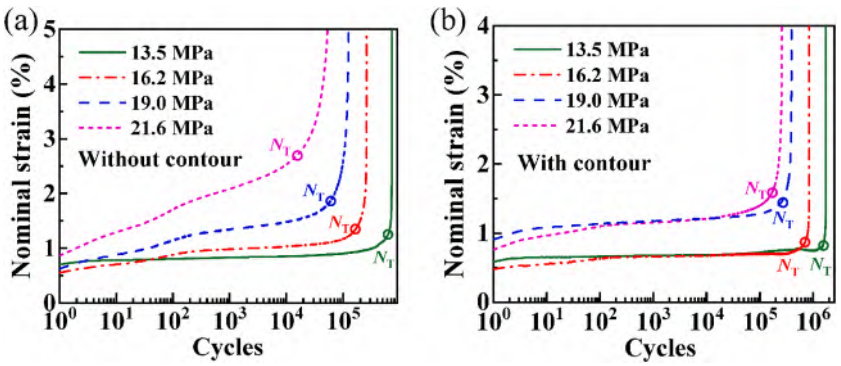

Fig. 12. Nominal strains plotted against loading cycle numbers for samples without (a) and with (b) contour scanning under cyclic nominal compressive stresses of 13.5 MPa, 16.2 MPa, 19.0 MPa, and 21.6 MPa.

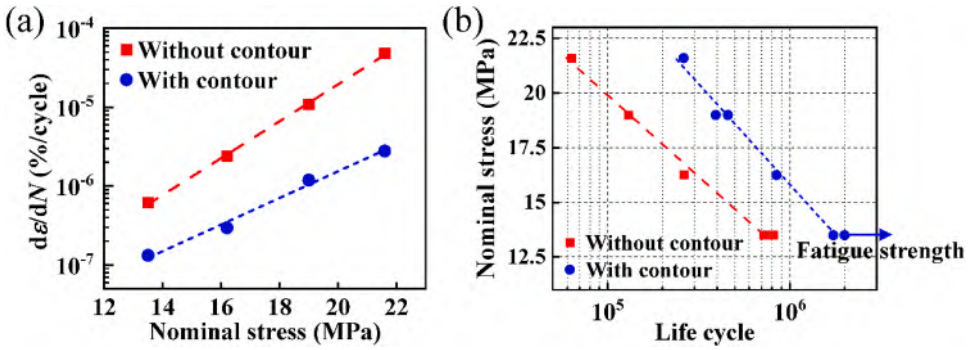

Fig. 13. (a) The nominal strain rates under various nominal stresses. (b) The fatigue life cycles versus nominal stresses for the gyroid samples without and with contour scanning.

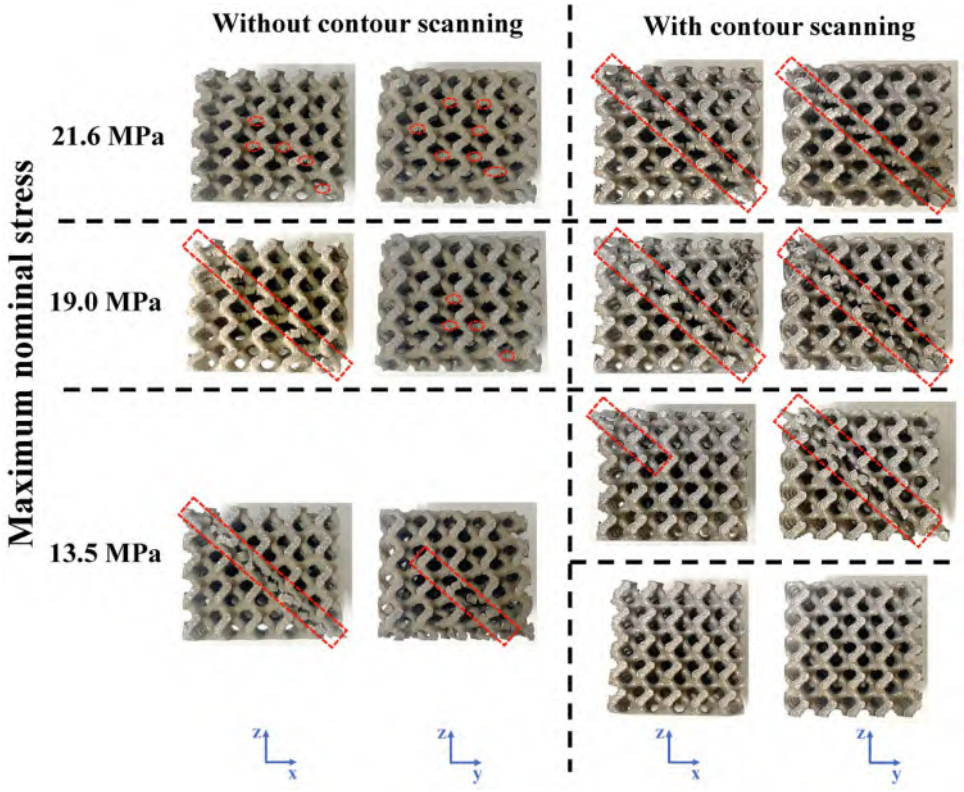

Fig. 14. Macroscopic failure behavior of the gyroid samples without and with contour scanning under compressive cyclic loads.

no apparent cracks at the run-out cycles (2×10^6), indicating that this maximum nominal stress serves as the fatigue strength. However, in other cases, the gyroid samples with contour scanning do exhibit clear 45° fracture bands in the inclined struts before reaching the run-out cycles. At the maximum nominal stress of 19.0 MPa, 45° fracture bands are observed in all samples. At a higher loading level (e.g., 21.6 MPa), the gyroid sample without contour scanning does not display 45° fracture bands; instead, it shows accumulated plastic deformation and local cracking of inclined struts, while the gyroid sample with contour scanning still exhibits the presence of fracture bands. This difference can be attributed to the improved plateau stress of the sample with contour scanning.

These observed failure behaviors somehow align with previous studies that identified a complex stress state—including tensile, shear, and torsional stresses—distributed around the oblique struts, leading to various fracture modes (I, II, III, and mixed-mode) in Ti6Al4V gyroid structures under compressive cyclic loading [21].

Fig. 15 shows that strut cracks initiate from surface irregularities, emphasizing the role of surface properties in determining fatigue performance. Overall, the struts in the sample with contour scanning display blunter notched regions for the crack initiation (Fig. 15d,e), compared to the struts without contour scanning (Fig. 15a,b). In the present study, crack initiation induced by the internal pores has not been observed, further emphasizing the significance of surface conditions for fatigue failure. Fig. 15c,f depicts the entire fracture surfaces of the struts, showcasing fatigue propagation and final rupture regions. The river patterns, reflective of fatigue crack propagation under cyclic loads, are observed.

5. Finite element analysis (FEA) of fatigue properties of lattice structures

To efficiently assess the fatigue behavior of the gyroid structures, FEA is performed on a single gyroid unit cell (Fig. 16). The material properties employed in the FEA model are Young's modulus E of 180 GPa, Poisson ratio of 0.3, and an isotropic hardening model. In the isotropic hardening model, the flow rule obeys $\mathrm{d}\boldsymbol{\varepsilon}^{\mathrm{pl}} = 3\mathbf{S}/\left(2\sigma_{\mathrm{eq}}\right)\mathrm{d}\bar{\varepsilon}^{\mathrm{pl}}$, where $\mathbf{S}$ is the deviatoric stress tensor, $\sigma_{\mathrm{eq}} = \left[(3/2)\mathbf{S} : \mathbf{S}\right]^{1/2}$ is the von Mises equivalent stress, and $\mathrm{d}\bar{\varepsilon}^{\mathrm{pl}} = \left[(2/3)\mathrm{d}\boldsymbol{\varepsilon}^{\mathrm{pl}} : \mathrm{d}\boldsymbol{\varepsilon}^{\mathrm{pl}}\right]^{1/2}$ is the scalar equivalent plastic strain rate with $\mathrm{d}\boldsymbol{\varepsilon}^{\mathrm{pl}}$ as the plastic strain rate tensor. The yield condition in the isotropic hardening model is $\sigma_{\mathrm{eq}} = q\left(\bar{\varepsilon}^{\mathrm{pl}}\right)$, where q is the hardening function of the scalar equivalent plastic strain $\bar{\varepsilon}^{\mathrm{pl}} = \int \mathrm{d}\bar{\varepsilon}^{\mathrm{pl}}$. For uniaxial loading, the above yield condition simplifies to $\sigma^{\mathrm{t}} = q(\varepsilon^{\mathrm{p}})$ with the uniaxial true plastic strain $\varepsilon^{\mathrm{p}} = \varepsilon^{\mathrm{t}} - \sigma^{\mathrm{t}}/E$. By interpolating the uniaxial true stress-true strain (σ^{t}-ε^{t}) curve in Fig. 2, the hardening function q is determined. Then the evolution of the true plastic strain and stress components in the gyroid unit cell is studied with FEA. The gyroid unit cell, with a size of 4 mm, is discretized using tetrahedral elements with an average size of 0.04 mm, which is significantly smaller than the minimum strut diameter of 1 mm. The mesh consists of over 9×10^5 elements, ensuring sufficient density to accurately capture the mechanical response of the structure. As

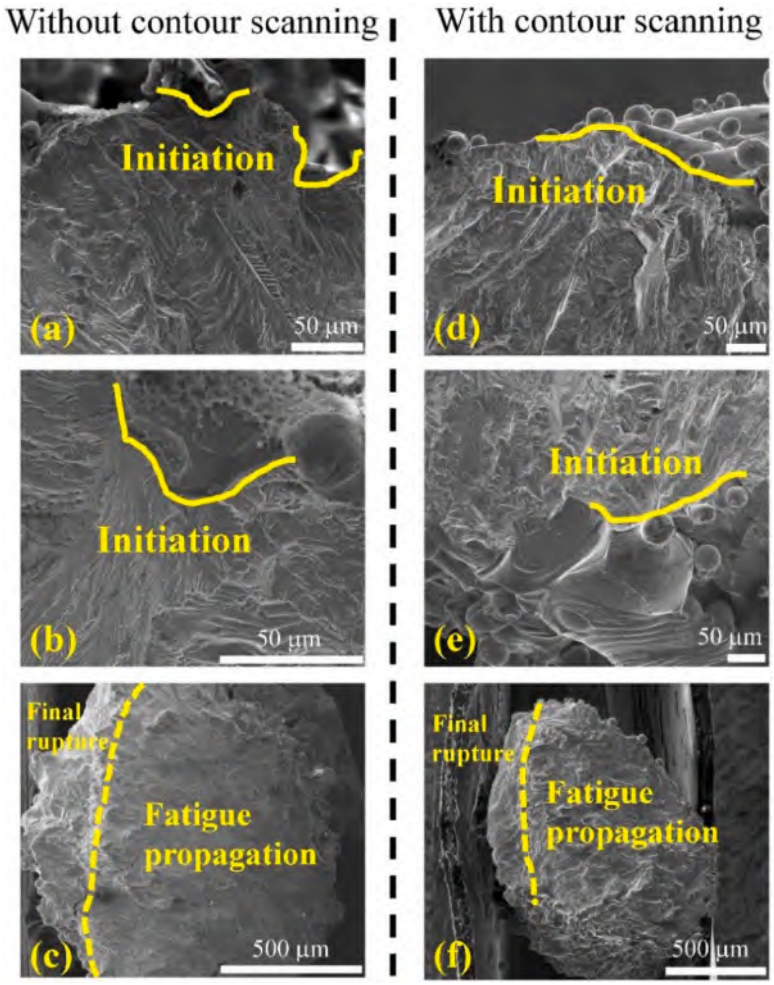

Fig. 15. (a,b), (d,e) Crack initiation regions of the struts of the gyroid samples without and with contour scanning. (c,f) Fracture surfaces of the struts. Fatigue initiation sites are indicated by solid yellow lines, while boundaries between the fatigue propagation and final rupture regions are marked with dashed yellow lines.

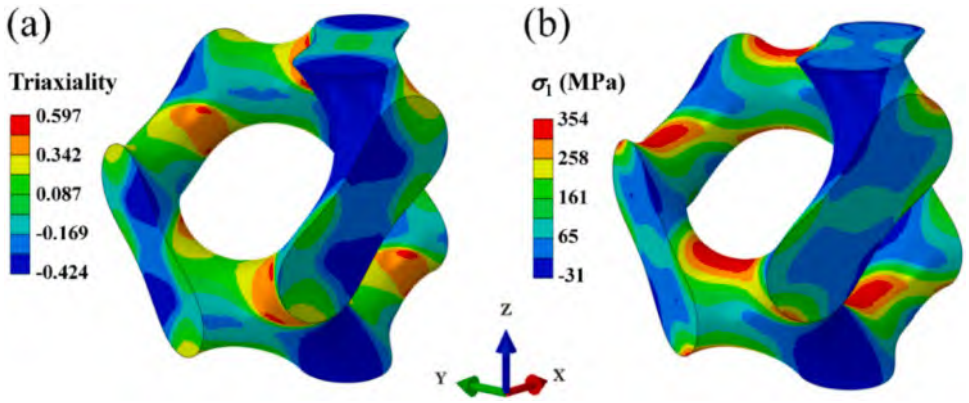

Fig. 16. Stress distribution in the gyroid unit cell under uniaxial compression (*z*-axis) at 19 MPa. (a) Stress triaxiality σ_m/σ_{eq} and (b) maximum true principal stress σ_1.

a result, element convergence analysis is not included in this study. Periodic boundary conditions for the displacements are applied to the unit cell in all three dimensions to simulate a continuous structure. In the case of uniaxial loading, only loading along the *z*-direction is applied.

Under uniaxial compression along the *z*-direction at 19 MPa (applied force divided by the unit cell's lateral area), Fig. 16a illustrates the stress distribution for the gyroid unit cell using stress triaxiality (σ_m/σ_{eq}, ratio of hydrostatic pressure σ_m to the von Mises equivalent stress σ_{eq}). Blue regions indicate dominant compression, green represents generalized shear, and yellow and red highlight localized tensile states at strut junctions and inclined struts. Furthermore, Fig. 16b shows the distribution of the corresponding maximum principal stress σ_1, confirming these localized tensile stresses. This distribution, when compared to failure behavior in Fig. 14, suggests that the inclined struts experiencing the highest tensile stresses are most vulnerable to initiating collapse of the entire structure.

The fatigue life of the gyroid structure under compression is predicted based on the simulated maximum principal stress distribution in Fig. 16b. The classical Basquin's equation relates the stress amplitude σ_a (Fig. 1c) and fatigue life N_f as [49]

$$\sigma_a = C_1 N_f^{C_2}, \tag{1}$$

where C_1 and C_2 are material constants. Here values of C_1 and C_2 are obtained from the fatigue data for tensile bars in Fig. 4 ($C_1 = 4622$ MPa and $C_2 = -0.286$ without contour scanning; $C_1 = 1628$ MPa and $C_2 = -0.182$ with contour scanning). With knowledge of C_1 and C_2, the fatigue life of the gyroid structure upon compression at the stress ratio $R = 0.1$ can be determined using Eq. (1), once the value of σ_a is determined. As the local tensile stress is detrimental to the fatigue resistance, here in the static compression FEA simulations for the gyroid structures, σ_a is taken as half the range of the maximum principal stress in the cell, that is, $\sigma_a = [\sigma_1(\sigma_{max}) - \sigma_1(\sigma_{min})]/2$. Here, σ_{max} and σ_{min} denote the applied maximum and minimum nominal stresses in the FEA simulations, respectively, which correspond to the peak and valley stresses in the fatigue loading curve in Fig. 1c when Eq. (1) is used. At $\sigma_{max} = 21.6$ MPa, 19 MPa, 16.25 MPa, and 13.5 MPa with $R = 0.1$ for the gyroid cells, corresponding values of the stress amplitude in the cells are $\sigma_a = 178.5$ MPa, 160.7 MPa, 132.4 MPa, and 105.9 MPa, respectively. Fig. 17 exhibits the predicted fatigue life cycle of the gyroid structure estimated using Eq. (1), which shows good agreement with the experimental results from Fig. 13b.

The numerical predictions using the principal stress method confirm the validity of assessing gyroid lattice fatigue resistance based on the fatigue properties of standard as-built specimens (fatigue bars). This approach eliminates the need for dedicated gyroid fatigue testing. As Fig. 17 demonstrates, contour scanning is an effective method for improving the fatigue performance of gyroid structures by minimizing surface defects.

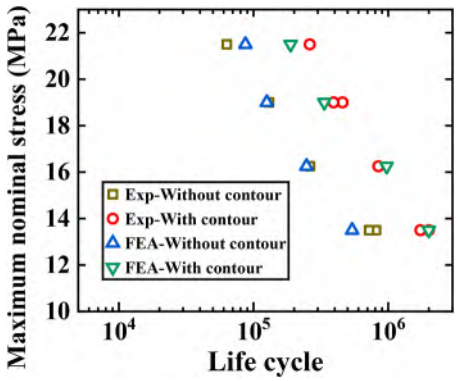

Fig. 17. Experimental results (from Fig. 13b) and FEA-based predictions of fatigue life cycles of the gyroid structure.

6. Further discussion

6.1. Enhancement of contour scanning

The layer-by-layer fabrication process with 33° rotation angle between layers inherently creates micronotches at the interface between neighboring layers due to the complex gyroid geometry. These sharp notches act as stress concentrators and can significantly reduce fatigue life. Border melting introduced by contour scanning smoothens these notches, significantly improving surface quality. As confirmed by the experimental results and simulations in Sections 3-5, the dominant factor for the enhanced fatigue properties of gyroid structures is this surface modification, rather than changes in microstructure. Our findings show that gyroid structures fabricated with contour scanning exhibit roughly three times longer fatigue life compared to those without (Fig. 17). This aligns with observations of the detrimental effect of surface notches on fatigue performance in additively manufactured Ti6Al4V thin-walled tubes [50].

Based on a simplified beam model, the cyclic damage is dD/dN, where $D = 1 - E^*/E$ is the scalar damage parameter with E^* and E representing the Young's moduli of the damaged material and the undamaged material without cracks, respectively. This relationship allows the cyclic damage to the gyroid struts under fatigue loading to be formulated as [47]

$$\frac{dD}{dN} = \frac{1}{\varepsilon_f}\frac{d(\varepsilon_c + \varepsilon_p)}{dN}.$$

Here, ε_f is the ductility of the undamaged constituent material, while ε_c and ε_p represent the cyclic ratcheting strain and cyclic plastic strain in the struts, respectively. The cyclic ratcheting strain per cycle $d\varepsilon_c/dN$ is derived using a creeping-beam model as [30,44]

$$\frac{d\varepsilon_c}{dN} = C_1(1-R)^p \frac{0.6}{n+2}\left[\frac{1.7(2n+1)}{n}\frac{\sigma_{LT}}{\sigma_0}\right]^n \overline{\rho}^{(3n+2)/2},$$

where R is the stress ratio, $\overline{\rho}$ is the relative density of the gyroid structure, σ_{LT} is the local maximum tensile stress in the strut, and C_1, p, n, and σ_0 are positive material constants. The cyclic plastic strain per cycle $d\varepsilon_p/dN$ is derived from the Coffin–Manson law as [47]

$$\frac{d\varepsilon_p}{dN} = C_2\varepsilon_y\left(\frac{\sigma_{LT}}{\overline{\rho}^2}\right)^m,$$

where ε_y is the monotonic yield strain of the undamaged constituent material, and C_2 and m are positive material constants. Consequently, the cyclic damage dD/dN is redefined as [30]

$$\frac{dD}{dN} = \frac{1}{\varepsilon_f}\left\{C_1(1-R)^p \frac{0.6}{n+2}\left[\frac{1.7(2n+1)}{n}\frac{\sigma_{LT}}{\sigma_0}\right]^n \overline{\rho}^{(3n+2)/2} + C_2\varepsilon_y\left(\frac{\sigma_{LT}}{\overline{\rho}^2}\right)^m\right\}.$$

This refinement reveals that cyclic damage accelerates with an increase in the local tensile stress within the structure, thereby promoting fatigue crack propagation. With the contour scanning, the maximum tensile stress on the rough surfaces of the gyroid structure can be mitigated, which in turn slows surface crack propagation and enhances fatigue performance.

6.2. Mechanical field

Under compressive loading, lattice struts typically undergo buckling and bending deformations. The ratcheting nominal strain rate in compression-compression fatigue is influenced by the ratio of buckling to bending components [45]. For instance, increasing the buckling component in a strut reduces the ratcheting nominal strain rate, thereby extending the fatigue life of rhombic dodecahedron lattices. The elastic deformation behavior of the gyroid lattice structures has been analytically investigated using a simplified beam model, showing that the inclined struts primarily bear loading through buckling and bending deformation [15]. The maximum axial tensile stress S in the simplified inclined strut under compressive force is given by [51]

$$S = F\frac{16L\cos\theta}{\pi d^3} - F\frac{4\sin\theta}{\pi d^2},$$

where F is the compressive force, L is the strut length, d is the strut diameter, θ is the angle between the strut and the loading plane. As the tensile stress in the strut is particularly detrimental to lattice fatigue fracture, reducing local tensile stress effectively enhances fatigue performance [52]. Increasing θ while maintaining L and d can decrease S, thereby improving fatigue resistance. In ref. [53], a novel structural design strategy is proposed to explore the anisotropic elastic properties of the gyroid structure by adjusting the force angle of the strut through the aspect ratio of the unit cell. This approach suggests that modifying θ via the gyroid cell aspect ratio can enhance fatigue performance, offering a promising direction for future studies.

7. Conclusions

This work investigates the impact of contour scanning on the fatigue properties of gyroid lattice structures fabricated using selective laser melting (SLM). Gyroid structures are manufactured with and without contour scanning, and their fatigue behavior is evaluated experimentally and numerically. The results clearly demonstrate the significant contribution of contour scanning in enhancing the fatigue resistance of the lattice structures.

Key findings reveal that gyroid struts fabricated without contour scanning exhibit surface defects like microcracks, voids, and notches. Conversely, structures built with contour scanning show a marked reduction in such imperfections. This improvement in surface quality translates to a notable enhancement in the compressive fatigue properties. For example, specimens fabricated with contour scanning exhibit a reduced nominal strain rate (per cycle) by orders of magnitude (from 10^{-4}~10^{-6} %/cycle to 10^{-6}~10^{-7} %/cycle) and a delayed fatigue endurance cycle by roughly three times (from 6×10^4~8×10^5 cycles to 2×10^5~2×10^6 cycles), compared to those fabricated without contour scanning. It is revealed that cyclic ratcheting remains the dominant fatigue mechanism in both cases, with fatigue damage driving the growth and coalescence of cracks. Importantly, the combined experimental and numerical analysis highlights the role of surface notches as crack initiation sites in the gyroid samples. By effectively mitigating these stress concentrators through contour scanning, this technique significantly improves fatigue resistance.

This work underscores the critical importance of minimizing surface defects in SLM-fabricated lattice structures to enhance fatigue endurance. Future research could focus on optimizing defect distribution through advanced fabrication techniques and post-treatments, as well as on developing high-fidelity numerical models based on CT-reconstructed geometries to improve fatigue prediction accuracy in complex SLM-fabricated structures.

CRediT authorship contribution statement

Liming Huang: Writing – original draft, Validation, Methodology, Investigation, Formal analysis. **Hongyuan Wan:** Investigation. **Quanfeng Han:** Investigation. **Jianxiang Wang:** Investigation. **Xin Yi:** Writing – review & editing, Validation, Supervision, Methodology, Investigation, Formal analysis, Conceptualization.

Declaration of competing interest

The authors declare that they have no known competing financial interests or personal relationships that could have appeared to influence the work reported in this paper.

Acknowledgments

This work was supported by the National Natural Science Foundation of China (grant no. 11988102). Computation resources supported by the High-performance Computing Platform of Peking University are acknowledged.

Data availability

Data will be made available on request.

References

[1] Pham MS, Liu C, Todd I, Lertthanasarn J. Damage-tolerant architected materials inspired by crystal microstructure. Nature 2019;565:305–11. https://doi.org/10.1038/s41586-018-0850-3.
[2] Zhang H, Wang Y, Kang Z. Topology optimization for concurrent design of layer-wise graded lattice materials and structures. Int J Eng Sci 2019;138:26–49. https://doi.org/10.1016/j.ijengsci.2019.01.006.
[3] Jin N, Wang F, Wang Y, Zhang B, Cheng H, Zhang H. Failure and energy absorption characteristics of four lattice structures under dynamic loading. Mater Des 2019;169:107655. https://doi.org/10.1016/j.matdes.2019.107655.
[4] Al-Saedi DSJ, Masood SH, Faizan-Ur-Rab M, Alomarah A, Ponnusamy P. Mechanical properties and energy absorption capability of functionally graded F2BCC lattice fabricated by SLM. Mater Des 2018;144:32–44. https://doi.org/10.1016/j.matdes.2018.01.059.
[5] Mahmoud D, Elbestawi MA. Lattice structures and functionally graded materials applications in additive manufacturing of orthopedic implants: A review. J Manuf Mater Process 2017;1:13. https://doi.org/10.3390/jmmp1020013.

[6] Wang L, Lau J, Thomas EL, MC Boyce. Co-continuous composite materials for stiffness, strength, and energy dissipation. Adv Mater 2011;23:1524–9. https://doi.org/10.1002/adma.201003956.
[7] Abueidda DW, Jasiuk I, Sobh NA. Acoustic band gaps and elastic stiffness of PMMA cellular solids based on triply periodic minimal surfaces. Mater Des 2018;145:20–7. https://doi.org/10.1016/j.matdes.2018.02.032.
[8] Al-Ketan O, Rowshan R, Abu Al-Rub RK. Topology-mechanical property relationship of 3D printed strut, skeletal, and sheet based periodic metallic cellular materials. Addit Manuf 2018;19:167–83. https://doi.org/10.1016/j.addma.2017.12.006.
[9] Sharma D, Hiremath SS. Additively manufactured mechanical metamaterials based on triply periodic minimal surfaces: performance, challenges, and application. Mech Adv Mater Struct 2022;29:5077–107. https://doi.org/10.1080/15376494.2021.1948151.
[10] Wang Y, Zhang X, Li Z, Gao H, Li X. Achieving the theoretical limit of strength in shell-based carbon nanolattices. Proc Natl Acad Sci USA 2022;119:e2119536119. https://doi.org/10.1073/pnas.2119536119.
[11] Maskery I, Sturm L, Aremu AO, Panesar A, Williams CB, Tuck CJ, Wildman RD, Ashcroft IA, Hague RJM. Insights into the mechanical properties of several triply periodic minimal surface lattice structures made by polymer additive manufacturing. Polymer 2018;152:62–71. https://doi.org/10.1016/j.polymer.2017.11.049.
[12] Abueidda DW, Elhebeary M, Shiang C-S, Pang S, Abu Al-Rub RK, Jasiuk IM. Mechanical properties of 3D printed polymeric gyroid cellular structures: experimental and finite element study. Mater Des 2019;165:107597. https://doi.org/10.1016/j.matdes.2019.107597.
[13] Wang P, Yang F, Li P, Zhang W, Lu G, Fan H. Bio-inspired vertex modified lattice with enhanced mechanical properties. Int J Mech Sci 2023;244:108081. https://doi.org/10.1016/j.ijmecsci.2022.108081.
[14] Wang P, Yang F, Zheng B, Li P, Wang R, Li Y, Fan H, Li X. Breaking the tradeoffs between different mechanical properties in bioinspired hierarchical lattice metamaterials. Adv Funct Mater 2023;33:2305978. https://doi.org/10.1002/adfm.202305978.
[15] Yang L, Yan C, Fan H, Li Z, Cai C, Chen P, Shi Y, Yang S. Investigation on the orientation dependence of elastic response in gyroid cellular structures. J Mech Behav Biomed Mater 2019;90:73–85. https://doi.org/10.1016/j.jmbbm.2018.09.042.
[16] Li X, Xiao L, Song W. Compressive behavior of selective laser melting printed gyroid structures under dynamic loading. Addit Manuf 2021;46:102054. https://doi.org/10.1016/j.addma.2021.102054.
[17] Bobbert FSL, Lietaert K, Eftekhari AA, Pouran B, Ahmadi SM, Weinans H, Zadpoor AA. Additively manufactured metallic porous biomaterials based on minimal surfaces: a unique combination of topological, mechanical, and mass transport properties. Acta Biomater 2017;53:572–84. https://doi.org/10.1016/j.actbio.2017.02.024.
[18] Kelly CN, Francovich J, Julmi S, Safranski D, Guldberg RE, Maier HJ, Gall K. Fatigue behavior of as-built selective laser melted titanium scaffolds with sheet-based gyroid microarchitecture for bone tissue engineering. Acta Biomater 2019;94:610–26. https://doi.org/10.1016/j.actbio.2019.05.046.
[19] Mahmoud D, Al-Rubaie KS, Elbestawi MA. The influence of selective laser melting defects on the fatigue properties of Ti6Al4V porosity graded gyroids for bone implants. Int J Mech Sci 2021;193:106180. https://doi.org/10.1016/j.ijmecsci.2020.106180.
[20] Yánez A, Fiorucci MP, Cuadrado A, Martel O, Monopoli D. Surface roughness effects on the fatigue behaviour of gyroid cellular structures obtained by additive manufacturing. Int J Fatigue 2020;138:105702. https://doi.org/10.1016/j.ijfatigue.2020.105702.
[21] Yang L, Wu S, Yan C, Chen P, Zhang L, Han C, Cai C, Wen S, Zhou Y, Shi Y. Fatigue properties of Ti-6Al-4V gyroid graded lattice structures fabricated by laser powder bed fusion with lateral loading. Addit Manuf 2021;46:102214. https://doi.org/10.1016/j.addma.2021.102214.
[22] Karami K, Blok A, Weber L, Ahmadi SM, Petrov R, Nikolic K, Borisov EV, Leeflang S, Ayas C, Zadpoor AA, Mehdipour M, Reinton E, Popovich VA. Continuous and pulsed selective laser melting of Ti6Al4V lattice structures: effect of post-processing on microstructural anisotropy and fatigue behaviour. Addit Manuf 2020;36:101433. https://doi.org/10.1016/j.addma.2020.101433.
[23] Qian W, Wu S, Lei L, Hu Q, Liu C. Time lapse in situ X-ray imaging of failure in structural materials under cyclic loads and extreme environments. J Mater Sci Technol 2024;175:80–103. https://doi.org/10.1016/j.jmst.2023.07.041.
[24] Wu Z, Wu S, Zhang J, Song Z, Hu Y, Kang G, Zhang H. Defect induced fatigue behaviors of selective laser melted Ti-6Al-4V via synchrotron radiation X-ray tomography. Acta Metall Sin 2019;55:811–20. https://doi.org/10.11900/0412.1961.2018.00408.
[25] Qian W, Wu S, Wu Z, Ahmed S, Zhang W, Qian G, Withers PJ. In situ X-ray imaging of fatigue crack growth from multiple defects in additively manufactured AlSi10Mg alloy. Int J Fatigue 2022;155:106616. https://doi.org/10.1016/j.ijfatigue.2021.106616.
[26] Ren Y, Li Y, Yang L, Chen Y, Yan C, Liu B, Cai X, Zhang M, Shi Y. Compressive properties and fatigue performance of NiTi lattice structures optimized by TPMS. Mater Sci Addit Manuf 2024;3:3380. https://doi.org/10.36922/msam.3380.
[27] Ravichander BB, Jagdale SH, Jabed A, Kumar G. Mechanical and corrosion behavior of sheet-based 316L TPMS structures. Int J Mech Sci 2023;254:108439. https://doi.org/10.1016/j.ijmecsci.2023.108439.
[28] Luo Z, Tang Q, Feng Q, Ma S, Song J, Setchi R, Guo F, Zhang Y. Finite element analysis of the mechanical properties of sheet- and skeleton-gyroid Ti6Al4V structures produced by laser powder bed fusion. Thin-Walled Struct 2023;192:111098. https://doi.org/10.1016/j.tws.2023.111098.
[29] Mishra AK, Chavan H, Kumar A. Effect of cell size and wall thickness on the compression performance of triply periodic minimal surface based AlSi10Mg lattice structures. Thin-Walled Struct 2023;193:111214. https://doi.org/10.1016/j.tws.2023.111214.
[30] Yang L, Yan C, Cao W, Liu Z, Song B, Wen S, Zhang C, Shi Y, Yang S. Compression–compression fatigue behaviour of gyroid-type triply periodic minimal surface porous structures fabricated by selective laser melting. Acta Mater 2019;181:49–66. https://doi.org/10.1016/j.actamat.2019.09.042.
[31] Jia H, Sun H, Wang H, Wu Y, Wang H. Scanning strategy in selective laser melting (SLM): a review. Int J Adv Manuf Technol 2021;113:2413–35. https://doi.org/10.1007/s00170-021-06810-3.
[32] Tian Y, Tomus D, Rometsch P, Wu X. Influences of processing parameters on surface roughness of Hastelloy X produced by selective laser melting. Addit Manuf 2017;13:103–12. https://doi.org/10.1016/j.addma.2016.10.010.
[33] Salman OO, Brenne F, Niendorf T, Eckert J, Prashanth KG, He T, Scudino S. Impact of the scanning strategy on the mechanical behavior of 316L steel synthesized by selective laser melting. J Manuf Processes 2019;45:255–61. https://doi.org/10.1016/j.jmapro.2019.07.010.
[34] Yu J, Kim D, Ha K, Jeon JB, Kim DJ, Lee W. Size effect due to contour laser scanning in 316L stainless steel produced by laser powder bed fusion. J Mater Res Technol 2021;15:5554–68. https://doi.org/10.1016/j.jmrt.2021.11.034.
[35] du Plessis A, Razavi SMJ, Berto F. The effects of microporosity in struts of gyroid lattice structures produced by laser powder bed fusion. Mater Des 2020;194:108899. https://doi.org/10.1016/j.matdes.2020.108899.
[36] Suard M, Martin G, Lhuissier P, Dendievel R, Vignat F, Blandin JJ, Villeneuve F. Mechanical equivalent diameter of single struts for the stiffness prediction of lattice structures produced by electron beam melting. Addit Manuf 2015;8:124–31. https://doi.org/10.1016/j.addma.2015.10.002.
[37] Hu YN, Wu SC, Withers PJ, Zhang J, Bao HYX, Fu YN, Kang GZ. The effect of manufacturing defects on the fatigue life of selective laser melted Ti-6Al-4V structures. Mater Des 2020;192:108708. https://doi.org/10.1016/j.matdes.2020.108708.
[38] Yang L, Ferrucci M, Mertens R, Dewulf W, Yan C, Shi Y, Yang S. An investigation into the effect of gradients on the manufacturing fidelity of triply periodic minimal surface structures with graded density fabricated by selective laser melting. J Mater Process Technol 2020;275:116367. https://doi.org/10.1016/j.jmatprotec.2019.116367.
[39] Han Q, Gu H, Soe S, Setchi R, Lacan F, Hill J. Manufacturability of AlSi10Mg overhang structures fabricated by laser powder bed fusion. Mater Des 2018;160:1080–95. https://doi.org/10.1016/j.matdes.2018.10.043.
[40] Wu SC, Yu C, Zhang WH, Fu YN, Helfen L. Porosity induced fatigue damage of laser welded 7075-T6 joints investigated via synchrotron X-ray microtomography. Sci Technol Weld Join 2015;20:11–9. https://doi.org/10.1179/1362171814Y.0000000249.
[41] Wang Q, Michaleris P, Nassar AR, Irwin JE, Ren Y, Stutzman CB. Model-based feedforward control of laser powder bed fusion additive manufacturing. Addit Manuf 2020;31:100985. https://doi.org/10.1016/j.addma.2019.100985.
[42] Casati R, Lemke J, Vedani M. Microstructure and fracture behavior of 316L austenitic stainless steel produced by selective laser melting. J Mater Sci Technol 2016;32:738–44. https://doi.org/10.1016/j.jmst.2016.06.016.
[43] Maskery I, Aboulkhair NT, Aremu AO, Tuck CJ, Ashcroft IA, Wildman RD, Hague RJM. A mechanical property evaluation of graded density Al-Si10-Mg lattice structures manufactured by selective laser melting. Mater Sci Eng A 2016;670:264–74. https://doi.org/10.1016/j.msea.2016.06.013.
[44] McCullough Fleck. The stress–life fatigue behaviour of aluminium alloy foams. Fatigue Fract Eng Mater Struct 2000;23:199–208. https://doi.org/10.1046/j.1460-2695.2000.00261.x.
[45] Zhao S, Li SJ, Hou WT, Hao YL, Yang R, Misra RDK. The influence of cell morphology on the compressive fatigue behavior of Ti-6Al-4V meshes fabricated by electron beam melting. J Mech Behav Biomed Mater 2016;59:251–64. https://doi.org/10.1016/j.jmbbm.2016.01.034.
[46] Zhou J, Soboyejo WO. Compression–compression fatigue of open cell aluminum foams: macro-/micro- mechanisms and the effects of heat treatment. Mater Sci Eng A 2004;369:23–35. https://doi.org/10.1016/j.msea.2003.08.009.
[47] Li SJ, Murr LE, Cheng XY, Zhang ZB, Hao YL, Yang R, Medina F, Wicker RB. Compression fatigue behavior of Ti–6Al–4V mesh arrays fabricated by electron beam melting. Acta Mater 2012;60:793–802. https://doi.org/10.1016/j.actamat.2011.10.051.

[48] Bowman SM, Guo XE, Cheng DW, Keaveny TM, Gibson LJ, Hayes WC, McMahon TA. Creep contributes to the fatigue behavior of bovine trabecular bone. J Biomech Eng 1998;120:647–54. https://doi.org/10.1115/1.2834757.
[49] Basquin OH. The exponential law of endurance tests. Proc Am Soc Test Mater 1910; 10:625–30.
[50] Zhang J, Fatemi A. Surface roughness effect on multiaxial fatigue behavior of additive manufactured metals and its modeling. Theor Appl Fract Mech 2019;103: 102260. https://doi.org/10.1016/j.tafmec.2019.102260.
[51] Van Hooreweder B, Apers Y, Lietaert K, Kruth J-P. Improving the fatigue performance of porous metallic biomaterials produced by selective laser melting. Acta Biomater 2017;47:193–202. https://doi.org/10.1016/j.actbio.2016.10.005.
[52] Liu Z, Gong H, Gao J. Enhancement in the fatigue resistances of triply periodic surfaces-based scaffolds. Int J Mech Sci 2023;245:108119. https://doi.org/10.1016/j.ijmecsci.2023.108119.
[53] Peng X, Huang Q, Zhang G, Li J, Zhang X, Lu Y, Jin Z. Compensating the anisotropic mechanical properties of electron beam melting-based gyroid scaffolds using structural design. Int J Mech Sci 2022;226:107442. https://doi.org/10.1016/j.ijmecsci.2022.107442.